ADVANCED FUNCTIONAL MATERIALS
www.afm-journal.de

Additive Manufacturing of High-Temperature Hybrid Electronics via Molecular-Decomposed Metals

Saurabh Khuje, Firas Alshatnawi, Detlef Smilgies, Mohammed Alhendi, Abdullah Islam, Jason Armstrong, Jian Yu, Mark Poliks,* and Shenqiang Ren**

As the modern electronic technology extends into operating in harsh working conditions, it calls for a system that is capable of uncompromising performance in extreme environments, thus providing a strong motivation to look for advanced materials and electronics with the capability of high-throughput and rapid prototyping. Coupled with additive manufacturing, molecular decomposition metals bypass the challenging oddities of traditional material-limited and thermally initiated metalworking, enabling high throughput and rapid prototyping of stoichiometry and composition-controlled metals. Here, a new paradigm for the design and additive manufacturing of copper metallic alloy materials onto ceramics is described by printing molecular decomposable metal materials, capable of withstanding thermo-mechanical loading, operating in extreme environments in static and dynamic conditions. The resulting printed hybrid electronics are electrically stable for 25 h of aging at 1000 °C. This curious fact paves a way for printed antenna and sensor electronics that reliably operate up to 1000 °C. These results can be further extended to establish other printable molecular decomposable materials as a platform for rapid prototyping of high temperature electronics that are suitable for harsh environments.

1. Introduction

Extreme environment electronics calls for advanced materials to function, with desirable futuristic capabilities relating to rocket propulsion, hypersonic flights or aerial vehicles, nuclear fusion,[1] deep seas, or outer planets[2] with conditions involving elevated temperatures, pressures, and mechanical or thermal shock. Additive manufacturing for printable electronics is favorably sought after due to its high-throughput and customization capabilities.[3–4] This paves a way toward understanding the response of materials when subjected to high-temperature conditions. An area that impedes state-of-the-art high temperature materials is the absence of intrinsic oxidation resistance, largely for said high-temperature applications. Hence, there is a need for developing materials for electronic applications in temperatures ranging from 600 to 1000 °C.[5] These extreme environments may affect material properties that involve phase transformations, oxidation, and corrosion characteristics.

Though metals are of considerable interest for electrical sensors and devices, high temperature electronics typically require a functional material capable of maintaining its electrical conductivity while simultaneously exhibiting high oxidation resistance, thus advancing a metal's oxidation resistance without compromising conductivity is crucial for harsh environments.[6] Copper (Cu) and copper alloys have been broadly utilized in electronic applications attributed to their high electrical and thermal conductivities,[7] and can prove to be an economical and environmentally-safe surrogate for tin–lead (utilized currently) and gold- or silver-based alloys (show promise) in packaging of electronics, if its oxidation can be arrested.[8] The metallic conductivity can be substantially reduced due to oxidation.[9,10] The passive coating prohibits corrosion on a deeper level, and usually

S. Khuje, A. Islam, S. Ren
Department of Materials Science and Engineering
University of Maryland
College Park, MD 20742, USA
E-mail: sren@umd.edu

The ORCID identification number(s) for the author(s) of this article can be found under https://doi.org/10.1002/adfm.202311085

DOI: 10.1002/adfm.202311085

F. Alshatnawi, D. Smilgies, M. Alhendi, M. Poliks
Department of Systems Science and Industrial Engineering
The State University of New York
Binghamton University
Binghamton, NY 13902, USA
E-mail: mpoliks@binghamton.edu

J. Armstrong
Department of Mechanical and Aerospace Engineering
The State University of New York
University at Buffalo
Buffalo, NY 14260, USA

J. Yu
DEVCOM Army Research Laboratory
Aberdeen Proving Ground, MD 21005, USA
E-mail: jian.h.yu.civ@army.mil

the thickness varies from a few nanometers to micrometers.[11,12] Nonetheless, it suffers from reduced conductivity at elevated temperatures, significantly limiting its usage. High-temperature oxidation of copper >1000 °C could be mitigated through material design and manufacturing controls. The addition of nickel (Ni) to Cu augments tensile strength and ductility,[13] as well as high corrosion resistance.[14,15] As a consequence, copper—nickel (CuNi) alloys are well-known for their high electrical, thermal conductivities and high oxidation resistance with applications spanning various fields.[14–16,17]

Herein, we describe the additive manufacturing of CuNi conductors via thermal decomposition of a mixture of copper-formate (CuF) and nickel formate (NiF) metal–organic decomposition (MOD) inks and its response in extreme environments by subjecting it to high-temperatures (≥1000 °C). The development of printable MOD inks,[18] which are substitutes for metallic nanoparticle inks, consisting of metal precursor solutions that are solely synthesized for printing purposes, with metallic cations bound by ligands, which can be further reduced by thermal decomposition to form metallic deposits as the ligand molecules are eliminated,[19,20] leading to an aggregated percolation network onto the printed substrate. This also allows for the stoichiometric variation of metallic precursors in the formulated inks. As MOD inks are essentially free of suspended particles, they can be smoothly extruded, thus avoiding clogging of the nozzle.[21] Here, we study the Cu—Ni-MOD ink characteristics, the effect of stoichiometric dependence on conductivity and high temperature resistance–temperature (R–T) performance, reliability at high temperature through aging along with the oxidation kinetics via in situ X-ray powder diffraction. Since the oxidation kinetics depend on the diffusion rate of oxygen through the conductor surface, the resulting alloy provides an electrical stability when aged for 25 h (resistivity of 0.14 Ω cm at 1000 °C for CuNi 1:1 for a sample dimension of 1.9 cm × 0.5 cm, and a thickness of 275 μm). The CuNi alloy is one of the materials that has the potential to be used as a temperature sensor for harsh environments.[22] This facilitates a method for printing and evaluating a Resistance–Temperature Detector (RTD) with reliable performance within a temperature range of 600–1000 °C and enabling a sensitivity of $0.32 \times 10^{-3}\ \Omega\ °C^{-1}$, and an antenna that is oxidation stable testing up to a temperature of 1000 °C with relatively negligible change in the antenna frequency.

2. Results and Discussion

Printable copper and nickel ink complexes, referred to as CuF-AMP (2-Amino-2-methyl-1-propanol) and NiF-AmIP (3-Aminopropanol or 1amino-2-propanol), are prepared via coordination of Cu and Ni salts with respective ligands. The metal ions can be reduced to their metallic counterparts by thermal decomposition by means of ligand-to-metal charge transfer subsequently after printing (**Figure 1**a).[23] The ink preparation involves the coordination of CuF with AMP and NiF with AmIP in molar ratios of 1:2 and 1:4, respectively. Both complexes can be defined in a similar fashion, with a metal ion center, two formate ligands and two amine ligands (Figure 1a). The rheological properties has been reported in our previous works.[24] The Cu(II)F, Ni(II)F, and amine complexes are produced when CuF and NiF salts are dissolved in amines, respectively, as described in Equation 1:[25]

$$\begin{aligned} &Cu(HCOO)_2 + 2R - NH_2 \rightarrow Cu(HCOO)_2(R - NH_2)_2 \\ &Ni(HCOO)_2 + 2R\prime - NH_2 \rightarrow Ni(HCOO)_2\left(R\prime - NH_2\right)_2 \end{aligned} \tag{1}$$

where R and R′ represent the carbon chains for AMP and AmIP, respectively. The decomposition of CuF occurs in two steps, the reduction of divalent Cu to monovalent Cu, followed by complete reduction of Cu, as shown in Equation 2:[26]

$$\begin{aligned} Cu^{II}(HCOO)_2 &\rightarrow Cu^{I}\,(HCOO) + CO_{2(g)} + 1/2H_{2(g)} \\ Cu^{I}\,(HCOO) &\rightarrow Cu_{(s)} + CO_{2(g)} + 1/2H_{2(g)} \end{aligned} \tag{2}$$

The reduction of NiF to Ni follows a similar process. After mixing the MOD inks together in varying stoichiometric ratios, they coordinate with each other via formation of hydrogen bonding. The contents of the ink are a result of conversion of Cu-Ni-MOD ink to CuNi alloy after thermal decomposition (Figure 1a). The subsequent printing process as well as the stoichiometric ratios that were studied are illustrated as well (Figure 1b). The ink was directly printed onto the ceramic substrates with desired patterns. One of the primary prerequisites for industry is a material capable of withstanding extreme environmental conditions for applications concerning sensing and communication. The high temperature electronic conductors as a result of CuNi alloy formation and the testing procedures are also depicted (Figure 1c). A rectangular patch antenna was printed with set dimensions and tested after sintering, using two distinct heat sources: a hydrogen torch and a furnace as shown in (Figure 1c top left and bottom left). The plot shows the antenna performance with the furnace as the heat source. At room temperature, the antenna displays a frequency of 0.84 GHz, with the S_{11} parameter value of −14.23 dB. When the antenna is placed inside the furnace at 1000 °C, the frequency stays the same, S_{11} changes to −13.52 dB, demonstrating that the printed CuNi antenna is stable at elevated temperatures, with negligible change in the S_{11} parameter (Figure S1, Supporting Information for antenna). The inset shows the schematic of the furnace being utilized for steady state characterization of the printed temperature sensor and antenna at high temperatures. This principle can be utilized for a global positioning system (GPS) antenna fabrication for hypersonic aerial vehicles (Movie S1 and Figure S2, Supporting Information). Applications for antenna have prerequisites such as extreme thermal shock resistance for missile applications, beyond line-of-vision communication for small to medium-sized unmanned aircraft systems for passive monitoring and communicating temperature[27] and pressure[28] under extreme environments as well as GPS applications.[29] High-temperature stability of printed CuNi conductors motivate the following studies to provide the mechanistic understanding of its oxidation resistance under high temperature conditions.

To efficiently convert printed Cu—Ni-MOD ink to an alloy conductor, pyrolysis studies were conducted with a temperature profile ranging from 300 to 1100 °C. The scanning electron microscopy (SEM) images of printed CuNi alloy pyrolyzed at 500 and 1100 °C with a dense percolation network was observed (**Figure 2**a,b). Figure S3 (Supporting Information) for SEM images for 300, 700, and 900 °C). It can be inferred that when the

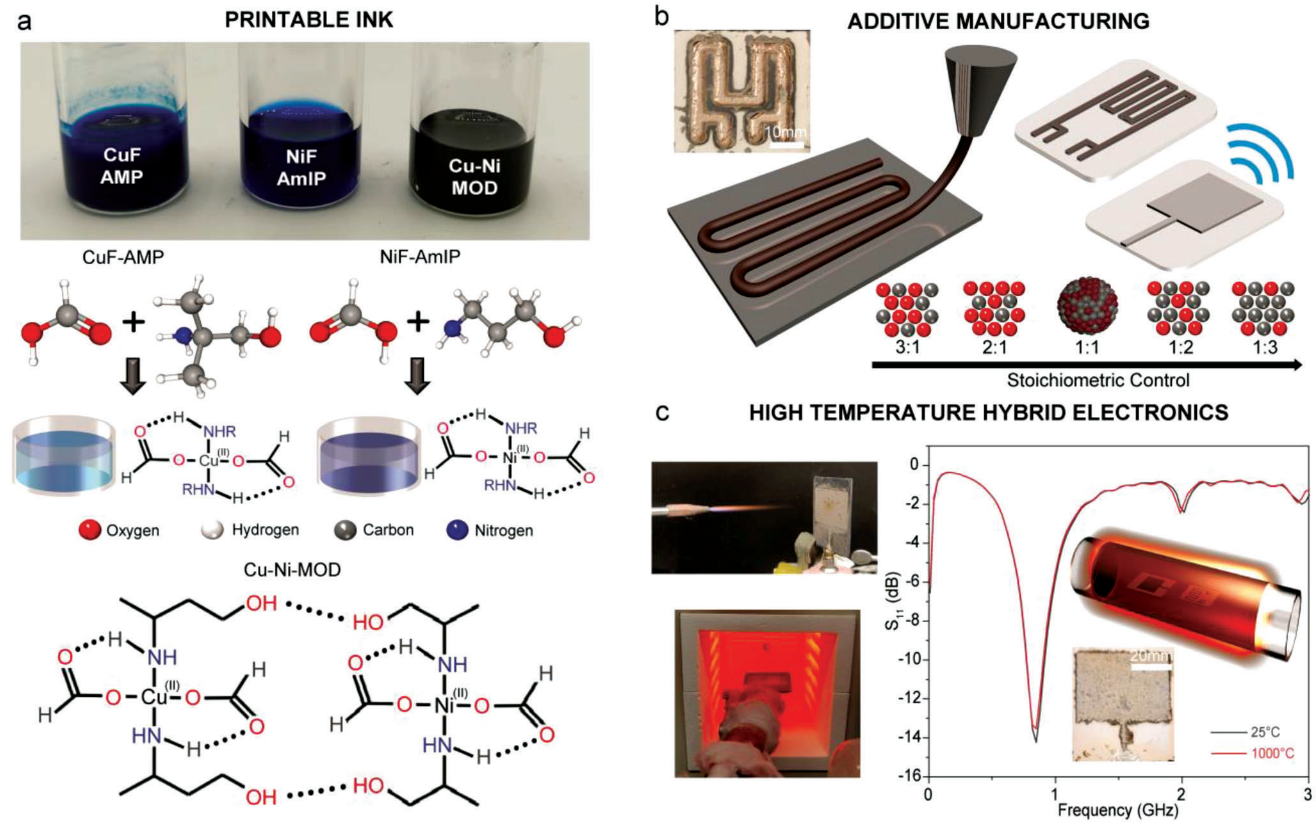

Figure 1. Schematics depict the experimental procedures followed in this study. a) Schematic depicting the printable ink preparation process. Top image displays the optical images of the prepared MOD inks. The latter section depicts the molecular structures of the MOD inks and the structure after mixing. b) Schematic depicting the additive manufacturing step of the process, with an optical image of the actual printed RTD sample. The bottom row depicts the various stoichiometric ratios studied (red═Cu, grayish silver═Ni). c) Schematic depicting the high temperature electronics testing using CuNi alloy. Plot depicting the antenna frequency at 25 and 1000 °C, indicating the stability with negligible changes to the S_{11} parameter.

pyrolysis temperature is lower (500 °C), an undesirable level of porosity of printed CuNi is resulted. Whereas a pyrolyzation temperature of 1100 °C is utilized to form a dense percolation network. The cross-section of the sample pyrolyzed at 1100 °C was observed under SEM to further elucidate the dense nature of the printed CuNi conductor (Figure 2c). The differential scanning calorimetry (DSC) studies for respective CuF-AMP and NiF-AmIP inks, as well as the Cu─Ni-MOD inks from the 1:1 mixture between CuF-AMP and NiF-AmIP were also conducted (Figure 2d). The decomposition of CuF-AMP takes place in two steps. For CuF-AMP, the peaks show up at 131 °C and 180°C, the first one representing the decomposition of CuF-AMP suggesting the formation of Cu(I) intermediate and the second of which represents the temperature required to reduce to Cu.[30] The inset shows thermal gravimetric analysis (TGA) of CuF-AMP, depicting the solid Cu content of 15.85%. For NiF-AmIP, two peaks show up at 142 and 239 °C while the former can be assigned to the decomposition of NiF-AmIP and the latter representing the temperature required to reduce the NiF-AmIP complex to metallic Ni.[31] It follows the same decomposition-reduction process as the CuF-AMP. The Cu─Ni-MOD peak lies between the two major peaks of CuF-AMP and NiF-AmIP, indicating a mixture of the two and that Cu can assist in catalyzing the reduction of NiF-AmIP at lower temperatures. The Cu can function as a seed for heterogenous nucleation of metal Ni ion as a result of decomposition of NiF-AmIP complex. The individual inks from the TGA analysis (inset, Figure 2d) have 15.52 wt.% Ni content, while the mixture shows 14.82 wt.% Cu─Ni content. The Fourier transform infrared spectroscopy (FTIR) was conducted for the individual amines, Cu- and Ni-MOD complexes as well as the Cu─Ni-MOD inks to further study the complexing characteristics (Figure 2e). Both CuF-AMP and NiF-AmIP have sharp peaks around 3000–3500 cm^{-1}, corresponding to N─H stretching bands (3000–3300 cm^{-1}) and C─H stretching bands (<3000 cm^{-1}), with the former confirming the presence of amines in the ink formulation.[24] For AMP, absorption peaks show up at 3343 and 3276 cm^{-1}, a result of symmetric and asymmetric stretching of NH_2 groups. The peaks at 2963 cm^{-1} are attributed to the asymmetric stretch of CH_3. The peak associated with 2870 cm^{-1} is related to the symmetric stretching mode of CH_2. After formulation of the CuF-AMP complex, the NH_2 peaks show a red shift, from 3343 cm^{-1} in AMP to 3283 cm^{-1} and 3276 cm^{-1} to 3149cm^{-1} in CuF-AMP. Additionally, a shift is observed in the peaks related to the carboxyl groups, from 1587 to 1569 cm^{-1} indicating formation of a free carboxyl group after dissociation of Cu^{2+} bonded carboxyl group.[32] These peak shifts indicate that AMP reacts with CuF, thus causing electron transfer from amine to Cu-ion, further reducing the density of electrons

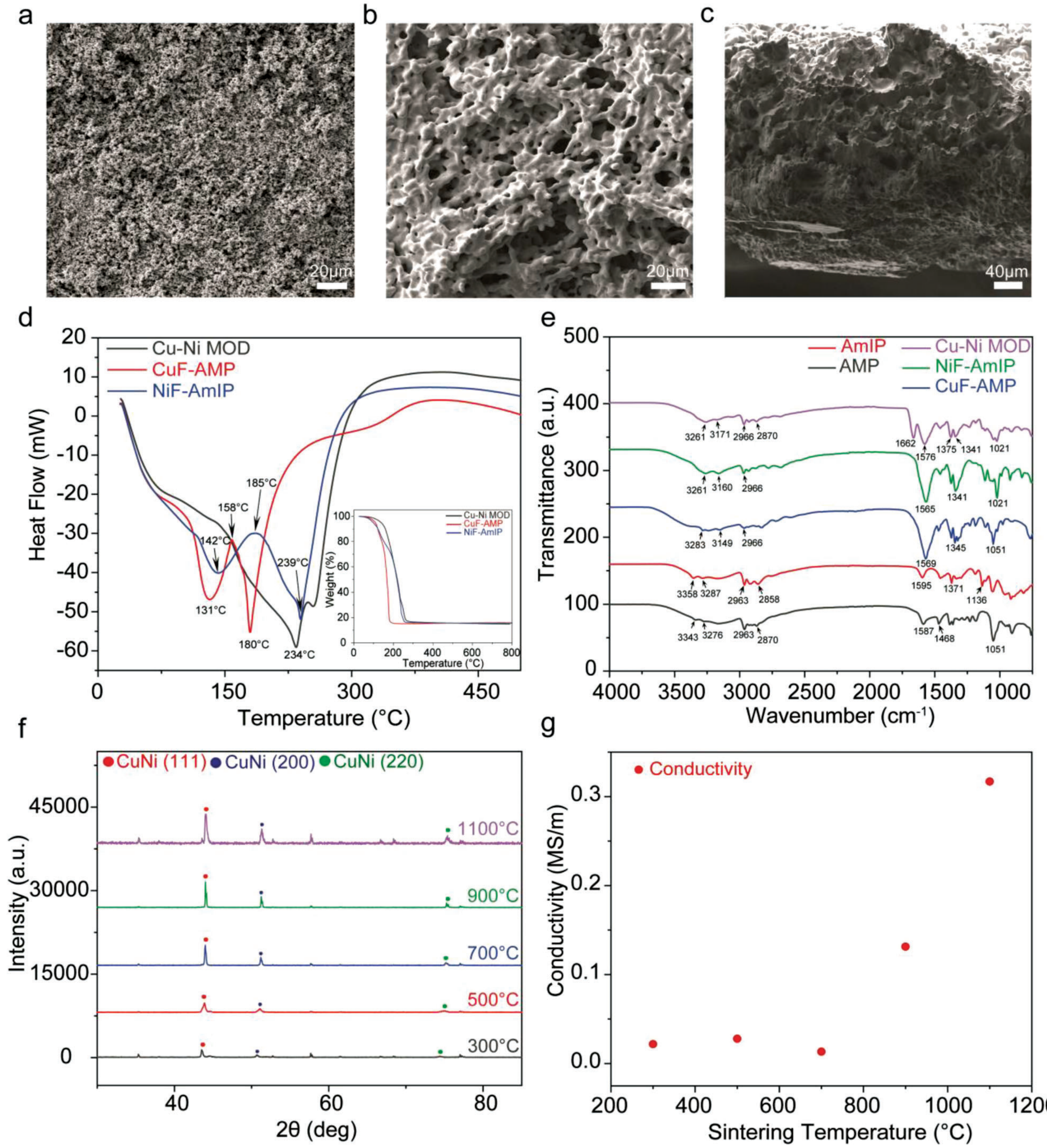

Figure 2. Characterization of MOD inks. a) SEM images for CuNi alloy sintered at 500 °C. b) SEM images for CuNi alloy sintered at 1100 °C. c) SEM image depicting the cross-section of sintered CuNi alloy. d) DSC curves for CuF-, NiF-, and Cu—Ni—MOD inks. Inset: TGA curves for CuF-, NiF-, and Cu—Ni—MOD inks. e) FTIR for individual amines and CuF-, NiF-, and Cu—Ni—MOD inks. f) Plot depicting XRD for MOD inks processed at different temperatures. g) Conductivity dependence on different processing temperatures for MOD inks.

of the amines and causing the reduction of metal Cu ion. Similar characteristic behavior is observed in NiF-AmIP complexes and Cu—NiMOD inks, where NH_2 and carboxyl peaks shift indicating the reduction of their respective metallic ions. Additionally, CuNi alloy (111), (200), and (220) peaks can be observed as a result of pyrolysis under forming gas (95% N_2, 5% H_2) at varying temperatures (Figure 2f). It is evident that as the temperature increases, the CuNi (111) peak intensity increases, indicating that the alloy develops preferentially in (111) plane with higher sintering temperatures assisting the formation of CuNi alloy. Similarly, the CuNi (200) and CuNi (220) peaks also arise prominently. For the FCC copper, the characteristic peaks appear at 43.3°, 50.4°,

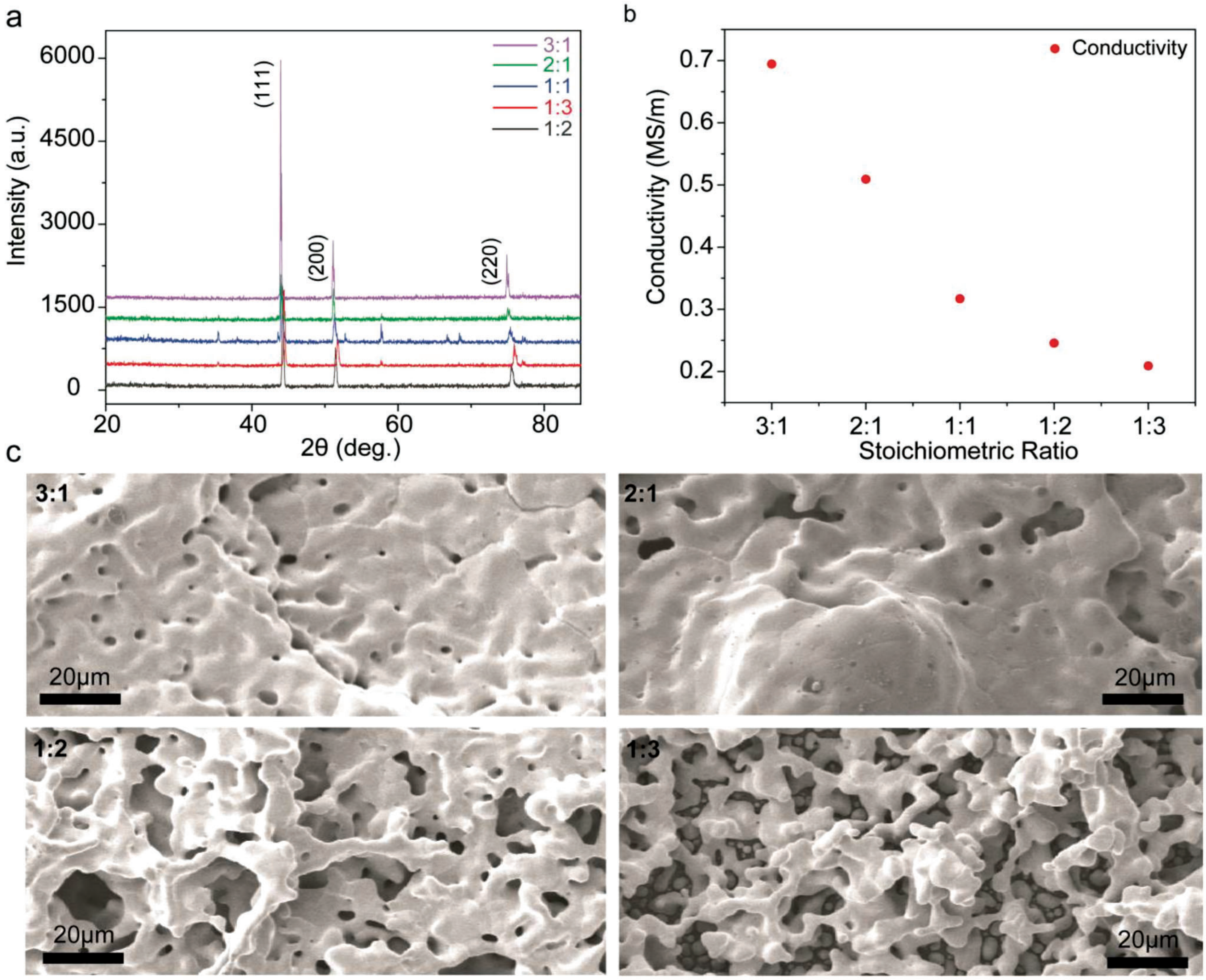

Figure 3. Stoichiometric ratio variation for CuNi alloy. a) Plot depicting the stoichiometric dependent XRD for CuNi alloys. b) The effect of stoichiometric composition on the conductivity of pyrolyzed CuNi alloy. c) SEM images depicting the percolated nanostructures for various stoichiometries (top left: 3:1, top right: 2:1, bottom left: 1:2, and bottom right: 1:3).

and 74.11° corresponding to (111), (200), and (220) planes.[33] For FCC nickel, characteristic peaks appear at 44.5°, 51.8°, and 76.41° corresponding to (111), (200), and (220) planes.[34] For the CuNi alloys, the 2θ shifts to 44.1°, 51.3°, and 75.4° corresponding to (111), (200), and (220) planes, respectively, suggesting the formation of CuNi alloy (Figure S4, Supporting Information, for CuNi Raman spectrum signifying the presence of amorphous carbon on the surface). The conductivity dependence on the processing temperature of printed CuNi conductors was characterized by using a four-point probe (Figure 2g). The electric conductivity remains the same (≈0.02 MS m^{-1}) if the processing temperature is below or 700 °C, due to the porosity in the network, but increases once the processing temperature is 900 °C (0.13 MS m^{-1}), with the sample processed at 1100 °C displaying the maximum conductivity (0.31 MS m^{-1}).

In order to achieve the oxidation stability without sacrificing electrical conductivity, various stoichiometric ratios were studied as the MOD inks allow for the stoichiometric ratio control. In order to determine the respective formation of a highly conductive and dense CuNi percolation network, we delve into the stoichiometric dependence of the Cu-Ni-MOD inks and the resulting alloys (**Figure 3**). The processed CuNi prepared using different stoichiometric ink ratios and their effect on resulting CuNi phases are studied using XRD (Figure 3a). It can be observed that lower the Cu content, the (111), (200), and (220) peaks for Ni dominant stoichiometric ratios (or lower Cu ratios) shift toward higher angles, stipulating an increase in the cell parameter, which agrees with Vegard's law.[35] The shift toward higher angles with increasing Ni content also indicates that Cu—Ni—MOD inks formed a CuNi alloy.[36] The XRD also elucidates the presence of pure CuNi solid solution (Figures S5–S8 (Supporting Information) for SEM and EDS of stoichiometric samples). For instance, Cu-dominant ink (3:1) has a peak closer to FCC Cu (111) that appears at 43.3° compared to Ni-dominant ink (1:3) that has a peak

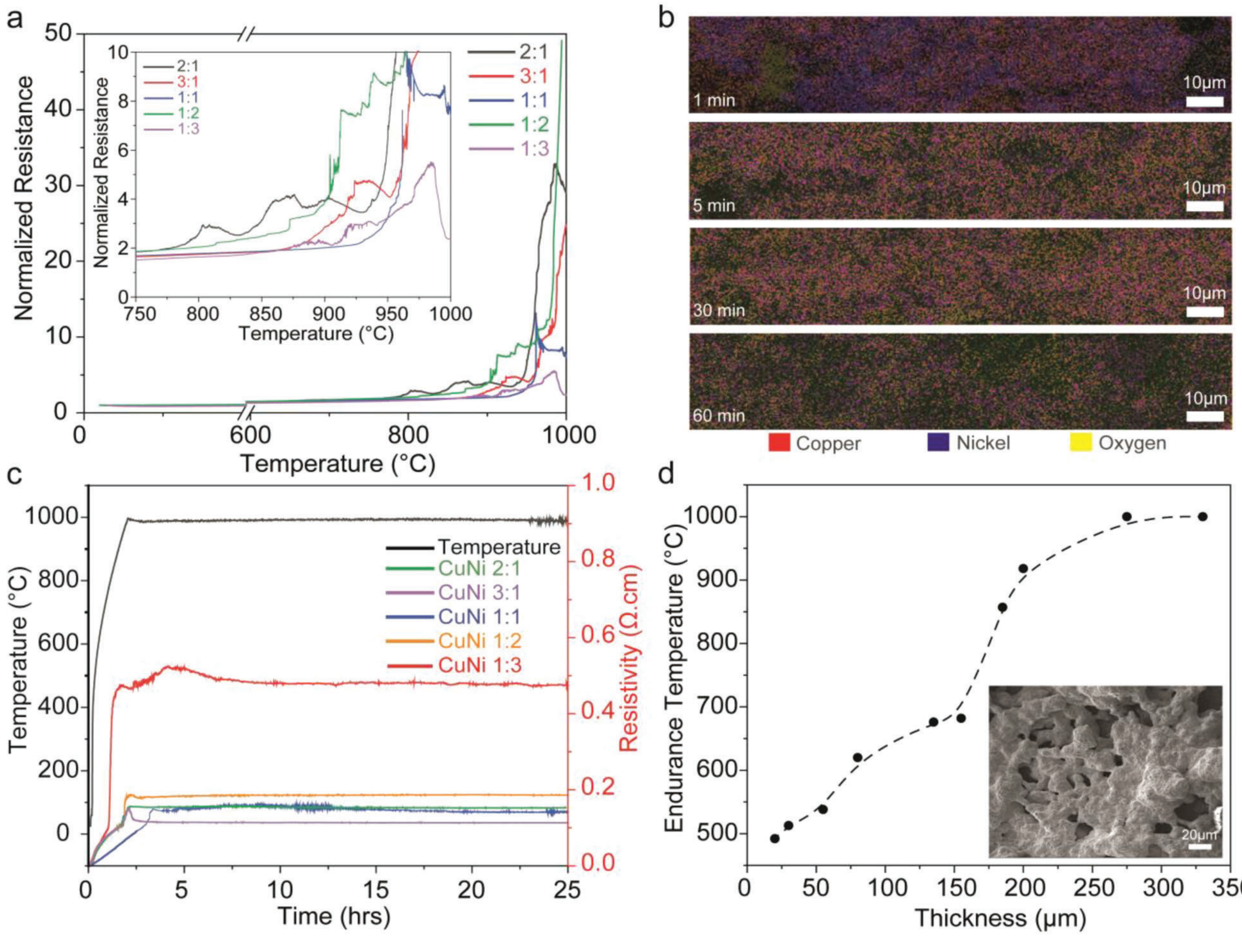

Figure 4. High temperature characterization of CuNi alloys. a) Plot depicting the R-T performance of various stoichiometric ratios. Inset: Zoomed-in view in the 750—1000 °C temperature range. b) EDS mapping for CuNi alloy aged at 1000 °C for varying times. c) Aging test for different stoichiometric ratios at 1000 °C for 25 h. d) Plot depicting the minimum thickness required for CuNi sample to endure 1000 °C.

closer to FCC Ni (111) at 44.5°. Regardless, all stoichiometric ratios show (111) peaks between Cu (111) and Ni (111) indicating the formation of CuNi alloy phase (similar results for peaks at (200) and (220)). The stoichiometric ratio dependent conductivity for printed CuNi alloys was further evaluated using a four-point probe (Figure 3b). It is evident from the plot that higher the copper molar ratio, higher is the conductivity (0.69 MS m^{-1} for CuNi ratio of 3:1), and as the nickel molar ratio increasing, the conductivity decreases (0.20 MS m^{-1} for CuNi ratio of 1:3), due to Ni being less conductive than that of copper (Cu = 5.96×10^7 S m^{-1}, Ni = 1.43×10^7 S m^{-1}). SEM observation of the different ratios of printed CuNi conductors processed at 1100 °C show the Cu-rich ratios forming a dense network whereas the Ni-rich ratios forming a porous network (Figure 3c).

It is necessary to evaluate high temperature electrical performance to determine the optimum stoichiometry for printed CuNi. The resistance-temperature characteristics of varying stoichiometric CuNi ratios up to 1000 °C in order to determine the oxidation initialization point was conducted under ambient conditions (**Figure 4**a). For the printed CuNi (molar ratio of 1:2) alloy, oxidation initiation starts ≈910 °C (change in normalized resistance from 1 to 5.12 Ω). Similarly, for the CuNi (2:1) oxidation initiation starts ≈948 °C (change in normalized resistance from 1 to 5.44 Ω), for CuNi (1:1) oxidation initiation starts ≈960 °C (change in normalized resistance from 1 to 4.78 Ω). For CuNi (3:1), oxidation initiation starts ≈924 °C (change in normalized resistance from 1 to 4.30 Ω) and the CuNi (1:3) survives over 1000 °C (change in normalized resistance from 1 to 2.37 Ω). It is to be noted that although the conductors show signs of oxidation initiation, they remain conductive throughout, and do not undergo complete degradation. A dense CuNi sample prepared via compacting CuNi sintered powder, and a melted sample prepared via heating CuNi sintered powder at 1300 °C were also evaluated for R–T characteristics (Figures S9 and S10 (Supporting Information) for R–T curve and cross-sectional SEM and EDS mapping for the dense sample, Figure S11 (Supporting Information) for R–T characteristic of the melted sample). SEM observation of CuNi was performed for increasing aging times at 1000 °C under ambient conditions, ranging from 1S to 60 min with EDS mapping overlayed in order to study the oxidation progression (Figure 4b). From the EDS mapping images, it can be perceived that after reaching 1000°C, an oxide layer forms on top of the CuNi and protects the sample from further oxidation, as the amount of oxidation remains the same as the

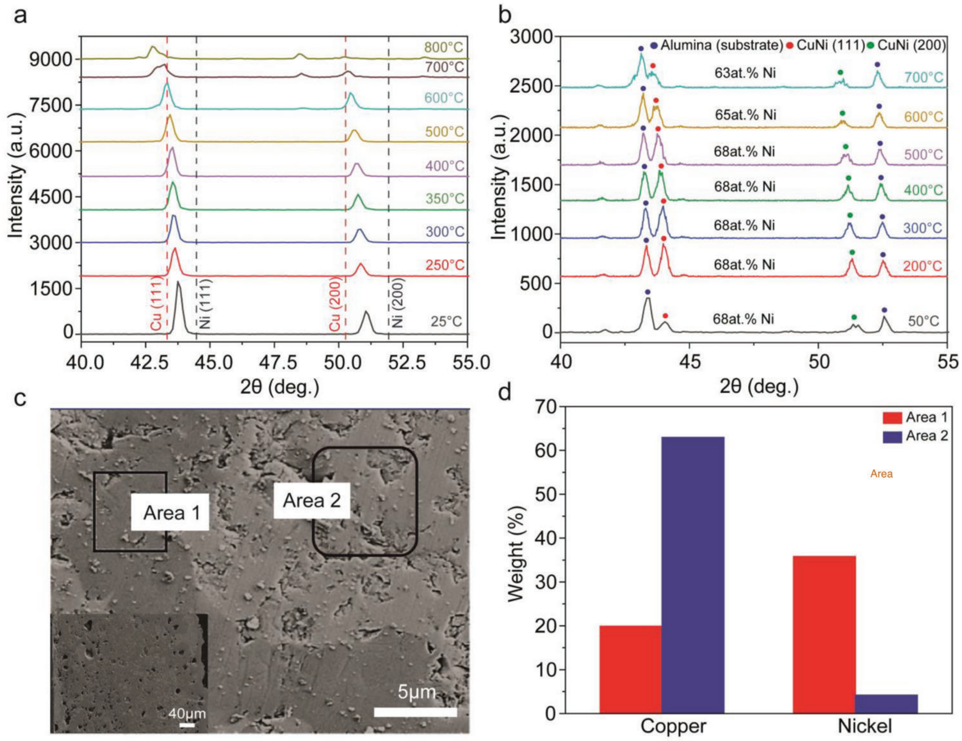

Figure 5. Oxidation kinetics for CuNi alloy. a) Plot depicting in-situ XRD for CuNi ratio 1:1 from 25° C to 800° C. (b) Plot depicting in-situ XRD for CuNi ratio 1:3 from 50 to 700 °C. c) SEM image showing phase separation at the cross-section following high temperature aging for CuNi 1:1. Inset: Morphological plane view of the aged CuNi sample at 1000 °C for 25 h. d) Bar chart depicting the EDS spectra for Cu and Ni presence in Area 1 and Area 2.

aging time increases (Figures S12–S16, Supporting Information, for cross-sectional SEM and EDS images of the sample after aging at 1000 °C for increasing duration). Prolonged aging tests of the different CuNi stoichiometric ratios was conducted to determine reliability at elevated temperatures under ambient conditions (Figure 4c). For CuNi 1:1 ratio, the resistivity increases and maintains a steady value of 0.14 Ω cm at 1000 °C. Similarly for other stoichiometric ratios of printed CuNi alloy conductors, the resistivity attains a set value and stabilizes at 1000 °C. A printed gold sample was utilized as control for aging test, with the sample beginning to show signs of oxidation around the 8-mark (Figure S17, Supporting Information). The thickness dependence of printed CuNi on its high temperature stability was also evaluated under ambient conditions (Figure 4d). A minimum thickness of 275 μm is crucial for the printed CuNi (1:1) to reliably operate at 1000 °C (Figure S18, Supporting Information for XRD of the sample before and after testing leading to failure at 1000 °C, Figure S19 (Supporting Information) for SEM images of the sample before and after testing at 1000 °C depicting oxidation by scale-like formation).

To determine the failure mechanism at elevated temperatures, in situ XRD of printed CuNi (1:1) conductors was performed (**Figure 5**a). As the temperature increases >500 °C, apart from thermal expansion a peak shift can be observed for CuNi (111) and CuNi (200) peaks as a result of continuous change in lattice constant as a function of composition, suggesting the phase separation of printed CuNi conductor. A minor peak emerges at 48.55 ° at 700 °C and 800 °C, corresponding to the formation of CuO layer, indicative of the initial oxide layer formation on top of the conductor (Figure S20, Supporting Information for TGA in air).[37] This CuO layer deposits on top of the copper alloy film and protects the copper matrix,[16,38] and thus helps maintain the electrical conductivity, resulting in a stable performance at 1000 °C. The in situ XRD of printed CuNi (1:3) conductor was also studied to further confirm the phase separation hypothesis (Figure 5b). At a temperature of 50°°C, distinct CuNi (111), (200), and alumina (substrate) peaks can be observed (Figure S21, Supporting Information for room temperature XRD of CuNi 1:3). Apart from linear thermal expansion the plots are identical and no variation in peak positions could be found <500°C. As the temperature reaches 600 °C, CuNi (111) peak shifts to 43.75 ° from the initial 44.05 °, suggesting phase separation being present in the mixture. It is to be noted that no CuO peak emerges as the temperature goes on increasing further (to 700 °C), which can be attributed to the increased stability provided by higher concentration of Ni in the CuNi 1:3 alloy. Additionally, the atomic percentage of Ni goes on decreasing, from 68% to 63% at 700 °C. The cross-sectional SEM image of the aged CuNi (1:1), with the inset showing the SEM image of the morphological plane view after aging the sample for 25 h at 1000 °C (Figure 5c). From the cross-section SEM, phase separation is evident attributing to the two distinct visible regions. A bar chart with the EDS mapping of the areas marked in Figure 5c, indicating phase separation in the two areas of the aged CuNi conductor, with Area 1 being Ni-rich and Area 2 being Cu-rich, further elucidating the phase separation at higher temperatures (Figure 5d). As phase separation initiates,

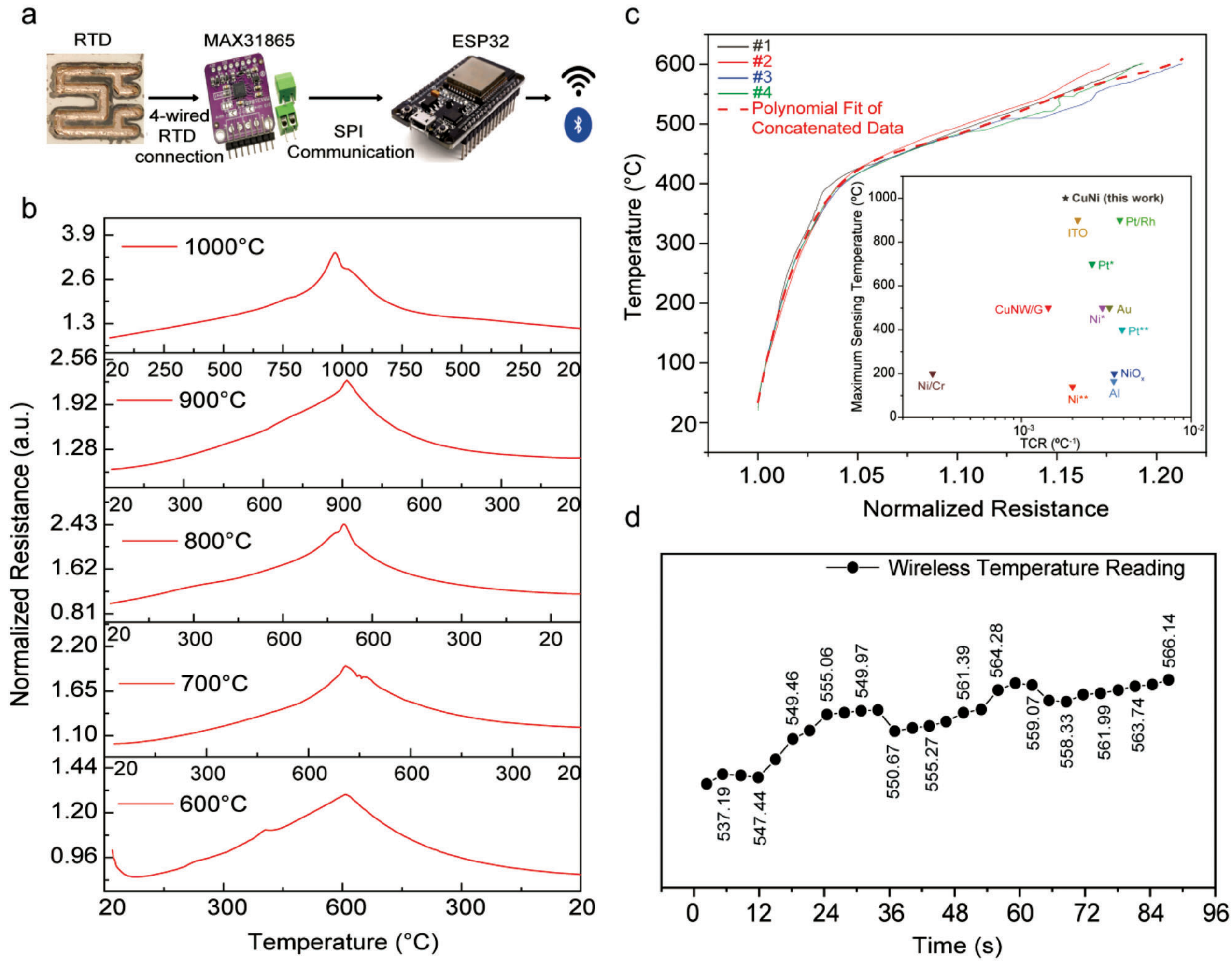

Figure 6. Resistance-based Temperature sensor testing. a) Schematic depicting the system consisting of data acquisition and wireless communication modules for the printed RTD. b) Plot depicting the RTD performance of CuNi 1:1 sample at various temperatures. c) The temperature versus normalized resistance plot for establishing polynomial relation between resistance and temperature. Inset: Ashby plot comparing the maximum sensing temperature versus temperature coefficient of resistance for RTDs reported in literature and this work (Ni/Cr,[43] CuNW/G,[44] Ni*,[45] Ni**,[46] Pt*,[47] Pt**,[48] Pt/Rh,[49] ITO,[50] Au,[51] NiO_x,[52] Al[53] and this work; CuNi). d) Plot depicting the data rendered in real-time from the webpage during the test, indicative of the temperature when the furnace was in the 535–570 °C range.

Cu is more susceptible to oxidation compared to Ni during high temperature testing under ambient conditions.

Recent demand for state-of-the-art high temperature sensor electronics for newer applications require specific parameters, especially concerned with satisfying the demands for monitoring chemical manufacturing plants, combustion turbines and engines, combustion reactors and agricultural waste processes, namely pyrolysis, boilers, furnaces, and heat pumps.[39] Printed high-temperature resistance-temperature detectors (RTDs) use the resistance variation of printed CuNi conductors with temperature change for temperature determination.[40] Similar to all other printed sensors, several factors need to be considered to achieve high temperature sensitivity, namely the material, configuration, resistance temperature coefficients (TCR), oxidation resistance, and manufacturing requirements.[41] Now that the printed CuNi alloy has been characterized for its R–T performance and oxidation kinetics, we demonstrate the use of CuNi as an RTD for high temperature applications. From the results presented above, we select CuNi 1:1 ratio for RTD study by printing CuNi onto alumina substrate (**Figure 6**) as it shows stable electric performance with high initial electrical conductivity (higher electrical conductivity compared to CuNi 1:3). A data acquisition and wireless communication system was utilized to effectively transmit data relating to the resistance and the corresponding temperature (Figure 6a). The MAX31865 amplifier board measures the resistance from the printed RTD device using a four-point connection, which allows the board to measure and rectify the lead resistance before each measurement. The board also consists of a 15-bit analog-to-digital converter (ADC) that helps in achieving an accuracy of 0.5 °C when connected to a standard 10 Ω platinum RTD (PT10). The amplifier board transfers the measured resistance to an ESP32 microcontroller using serial peripheral interface (SPI) communication, which in turn converts the resistance to a temperature measurement using a calibration function provided by an equation relating resistance and temperature in the Arduino code. The ESP32 follows protocols 802.11 b g^{-1} n^{-1} for Wi-Fi, enabling wireless connectivity and deeming it ideal for wireless communication. An exponential filter was used to eliminate the noise, which also affects the sensor response time as a result. This filter implements a simple linear recursive exponential filter for the Arduino module and provides a simplified method to smooth noise from measurements without the intensive need of memory as a moving average filter. The performance of printed CuNi alloy at varying temperatures, ranging from 600 to 1000 °C was evaluated (Figure 6b; Movie S2, Supporting Information). Is evident that the curve displays a positive temperature coefficient and a reversible trend throughout all the runs (with minor changes in the initial resistance due to onset of oxidation), thus displaying thermal cyclability of the CuNi alloy based RTD. The positive trend agrees with metallic conductors and can be utilized to determine the temperature coefficient of resistance (*TCR*, α), defined as relative resistance change per degree measured, established by the formula $R_2 = R_{1\times}[1 + \alpha(T_2 – T_1)]$, where T_1 and T_2 are the initial and final temperatures and R_1 and R_2 are the initial and final resistances. The sensitivity (S), which is a product of the initial resistance and the TCR. The α value for the 600 °C run is 0.50×10^{-3} °C^{-1}, with $S = 0.6 \times 10^{-3}$ Ω °C^{-1}. Similarly, for 700 °C, $\alpha = 1.39 \times 10^{-3}$ °C^{-1}, with $S = 1.42 \times 10^{-3}$ Ω °C^{-1}. For 800 °C, $\alpha = 1.80 \times 10^{-3}$ °C^{-1}, with $S = 2.49 \times 10^{-3}$ Ω °C^{-1}. For 900 °C, $\alpha = 1.35 \times 10^{-3}$ °C^{-1}, with $S = 1.43 \times 10^{-3}$ Ω °C^{-1}. For 1000 °C, $\alpha = 1.82 \times 10^{-3}$ °C^{-1}, with $S = 1.88 \times 10^{-3}$ Ω °C^{-1}. A gold RTD was printed and utilized as a control sample for RTD measurements (Figure S22, Supporting Information). As this experiment showed the ability of the CuNi conductor to function as a temperature sensor reliably at different temperatures, we go a step further and establish an Arduino board to test the wireless RTD capability. A concatenated curve-fit was employed for four cyclic runs up to 600 °C to calculate the exponents that are to be plugged into the Arduino code in order to get updates in real time on the developed webpage (Figure 6c; Movie S3, Supporting Information). It is to be noted that as prolonged exposure at higher temperatures result in phase separation between Cu and Ni, the multiple runs for the RTD were restricted to a temperature of 600 °C for the RTD application. Figure 6c inset shows the Ashby plot comparing the maximum sensing temperature versus temperature coefficient of resistance for different RTDs reported in literature and this work (Table S1, Supporting Information for values). A fifth order polynomial fit was utilized to obtain an equation for temperature in terms of resistance in the form $T = C + B_1R + B_2R^2 + B_3R^3 + B_4R^4 + B_5R^5$, where T is temperature and R is the resistance and B representing the corresponding coefficients, and C is the intercept. Here, $C = 3.13 \times 10^9$ and $B_1 = -15 \times 10^9$, $B_2 = 28.74 \times 10^9$, $B_3 = -27.52 \times 10^9$, $B_4 = 1.31$, and $B_5 = -2.52 \times 10^9$. The corresponding temperature measurement for a certain extent when the furnace was within a temperature range of 535–570 °C as displayed by the server on the webpage was captured and plotted (Figure 6d). The α value for this wireless sensor is 0.33×10^{-3} °C^{-1}, and $S = 0.32 \times 10^{-3}$ Ω °C^{-1}.

3. Conclusion

In this study, we present high-temperature hybrid electronics using the printed CuNi conductors formed via thermal decomposition of CuF and NiF molecular decomposable inks. The printed CuNi alloy conductors with stoichiometry control provide a stable electrical performance at 1000 °C under 25 h of aging. This was utilized to develop a printed temperature sensor, that can reliably function in the temperature range of 600–1000 °C with a sensitivity of 0.32×10^{-3} Ω °C^{-1}. The printed high temperature antenna was also investigated, by subjecting the antenna to steady and dynamic high temperature states (≥ 1000 °C), with the antenna maintaining its frequency under both circumstances, further proving the stability of formulated CuNi alloys. This work opens an extensive path for future research with printable MOD inks and additive manufacturing, creating conductors that are electrically stable and oxidation resistant, which can enable applications for harsh environments.

4. Experimental Section

Copper—Nickel (Cu—Ni) MOD Ink Preparation: For synthesis of CuNi-MOD, CuF was mixed with AMP in a molar ratio of 1:2 and then centrifuged in Thinky Mixer ARE-310 for 8 min. Extensive studies on CuF-AMP MOD has been done in one of our recent works.[42] Independently, nickel formate (NiF) was mixed with 1-amino-2-propanol (AmIP) ligand in a molar ratio of 1:4, with subsequent centrifugation in Thinky Mixer for achieving a uniform mixture. CuF- and NiF-MODs were then mixed together at a 1:1 Cu:Ni molar ratio (e.g., 3.14 g of CuF-AMP MOD and 2.6 g NiF-AmIP MOD) to make CuNi-MOD.[31] Similarly, for other stoichiometries, solutions were mixed accordingly. The ink mixture was heated on a hot plate in a glove box at a temperature of 300 °C to obtain Cu-Ni nanoparticles. This nanoparticle mixture was filtered through a 165 µm mesh and directly used for printing the test samples.

High Temperature Processing and Characterization: The samples were printed using Voltera V-One, an extrusion-based printer utilizing direct-writing technique onto pre-etched ceramic substrates. The sample were then pyrolyzed via a two-step sintering process. The first step involves heating the samples in a box furnace under nitrogen environment at a temperature of 300 °C for a duration of 30 min with a ramping rate of 10 °C min^{-1} and allowing natural cooling. For the second pyrolysis step, a tube furnace was employed, with the samples being pyrolyzed at individual temperature ranges of 300–1100°C for a duration of 30 min under an inert atmosphere (forming gas, 95% N_2, 5% H_2), with a ramping rate of 5 °C min^{-1} and allowing natural cooling. Electrical conductivities were obtained via a four-point probe. The electrical stability measurements were measured using a Keithley 2450 Sourcemeter and a box furnace as a heating source, with platinum wires as electrodes and a ramping rate of 5 °C min^{-1}.

In Situ XRD: High-temperature in situ XRD characterization was performed on a PANalytical X'Pert Pro diffractometer using an Anton Paar DHS 900 high temperature stage (Analytical and Diagnostics Laboratory at Binghamton University).

Supporting Information

Supporting Information is available from the Wiley Online Library or from the author.

Acknowledgements

Financial support was provided by the DEVCOM Army Research Laboratory supports S. R. under Award W911NF-20-2-0016 (conductive ink materials). This material (high temperature printable resistance-temperature sensor electronics) was based on research sponsored by the Air Force Research Laboratory under Agreement Number FA8650-20-2-5506. The U.S. Government is authorized to reproduce and distribute reprints for Governmental Purposes notwithstanding any copyright notation thereon. The views and conclusions contained herein were those of the authors and should not be interpreted as necessarily representing the official policies or endorsements, either expressed or implied, of Air Force Research Laboratory or the U.S. Government.

Conflict of Interest

The authors declare no conflict of interest.

Author Contributions

The manuscript was written through contributions of all authors. S.R and J.Y. designed and supervised the project. S.K worked on the synthesis of Cu—Ni-MOD alloys and the printable ink preparation and electronic characterization. S.K. and A.I. worked on the machining of ceramics. F.A., M.A., D.S., and M.P. contributed to the reliability testing of the printed resistance temperature sensor electronics and X-ray diffraction studies. J.A. contributed to the design and construction of wireless communication modules.

Data Availability Statement

The data that support the findings of this study are available from the corresponding author upon reasonable request.

Keywords

antenna, copper—nickel, extreme environments, high temperature, printable electronics, temperature sensors

Received: September 13, 2023
Published online: October 20, 2023

[1] L. Feng, W. G. Fahrenholtz, D. W. Brenner, *Annu. Rev. Mater. Res.* **2021**, *51*, 165.
[2] A. P. Siciliano, University of Maryland, College Park, **2021**.
[3] A. H. Espera, J. R. C. Dizon, Q. Chen, R. C. Advincula, *Progress in Additive Manufacturing* **2019**, *4*, 245.
[4] X. Zeng, P. He, M. Hu, W. Zhao, H. Chen, L. Liu, J. Sun, J. Yang, *Nanoscale* **2022**, *14*, 16003.
[5] B. A. Pint, *Mater. Sci. Technol.* **2014**, *30*, 1387.
[6] K. Lu, *Science* **2010**, *328*, 319.
[7] J. R. Davis, *Copper and copper alloys*, ASM international, Almere **2001**.
[8] J. Song, L. Wang, A. Zibart, C. Koch, *Metals* **2012**, *2*, 450.
[9] M. A. Cruz, S. Ye, M. J. Kim, C. Reyes, F. Yang, P. F. Flowers, B. J. Wiley, *Part. Part. Syst. Charact.* **2018**, *35*, 1700385.
[10] C. Yim, Z. A. Kockerbeck, S. B. Jo, S. S. Park, *ACS Appl. Mater. Interfaces* **2017**, *9*, 37160.
[11] D. Landolt, *Corrosion and surface chemistry of metals*, EPFL press, Lausanne **2007**.
[12] S. Khuje, F. Alshatnawi, M. Alhendi, J. Yu, A. Sheng, Y. Huang, C. G. Zhuang, J. Armstrong, C. Zhou, M. Poliks, *Adv. Electron. Mater.* **2022**, *9*, 2200979.
[13] A. D. Pingale, S. U. Belgamwar, J. S. Rathore, *Bull. Mater. Sci.* **2020**, *43*, 66.
[14] J. Chen, Z. Li, A. Zhu, L. Luo, J. Liang, *Mater. Des.* **2012**, *34*, 618.
[15] S. J. Yuan, S. O. Pehkonen, *Corros. Sci.* **2007**, *49*, 1276.
[16] S. J. Yuan, A. M. F. Choong, S. O. Pehkonen, *Corros. Sci.* **2007**, *49*, 4352.
[17] W. Li, L. Li, F. Li, K. Kawakami, Q. Sun, T. Nakayama, X. Liu, M. Kanehara, J. Zhang, T. Minari, *ACS Appl. Mater. Interfaces* **2022**, *14*, 8146.
[18] Y. Rosen, M. Grouchko, S. Magdassi, *Adv. Mater. Interfaces* **2015**, *2*, 1400448.
[19] C. E. Knapp, J.-B. Chemin, S. P. Douglas, D. A. Ondo, J. Guillot, P. Choquet, N. D. Boscher, *Adv. Mater. Technol.* **2018**, *3*, 1700326.
[20] C. E. Knapp, E. A. Metcalf, S. Mrig, C. Sanchez-Perez, S. P. Douglas, P. Choquet, N. D. Boscher, *ChemistryOpen* **2018**, *7*, 850.
[21] Y.e Zhou, Z. Xu, H. Bai, C. E. Knapp, *Adv. Mater. Technol.* **2023**, *8*, 2201557.
[22] B. W. An, J. H. Shin, S.-Y. Kim, J. Kim, S. Ji, J. Park, Y. Lee, J. Jang, Y.-G. Park, E. Cho, *Polymers* **2017**, *9*, 303.
[23] D.-H. Shin, S. Woo, H. Yem, M. Cha, S. Cho, M. Kang, S. Jeong, Y. Kim, K. Kang, Y. Piao, *ACS Appl. Mater. Interfaces* **2014**, *6*, 3312.
[24] A. Sheng, A. Islam, S. Khuje, J. Yu, H. Tsang, A. Bujanda, S. Ren, *Chem. Commun.* **2022**, *58*, 9484.
[25] Y.-H. Choi, S.-H. Hong, *Langmuir* **2015**, *31*, 8101.
[26] A. K. Galwey, D. Jamieson, M. E. Brown, *J. Phys. Chem.* **1974**, *78*, 2664.
[27] H. Cheng, S. Ebadi, X. Ren, X. Gong, *Sens. Actuators, A* **2015**, *222*, 204.
[28] Q. Tan, T. Luo, T. Wei, J. Liu, L. Lin, J. Xiong, *J. Microelectromech. Syst.* **2017**, *26*, 351.
[29] Y. Liu, S. Zhang, Y. Gao, *Adv. Electron. Mater.* **2016**, *16*, 1397.
[30] Y. Farraj, M. Grouchko, S. Magdassi, *Chem. Commun.* **2015**, *51*, 1587.
[31] D. Tomotoshi, R. Oogami, H. Kawasaki, *ACS Appl. Mater. Interfaces* **2021**, *13*, 20906.
[32] W. Yang, C. Wang, V. Arrighi, *J. Mater. Sci.: Mater. Electron.* **2019**, *30*, 11607.
[33] J. Ramyadevi, K. Jeyasubramanian, A. Marikani, G. Rajakumar, A. A. Rahuman, *Mater. Lett.* **2012**, *71*, 114.
[34] H. Wang, X. Kou, J. Zhang, J. Li, *Bull. Mater. Sci.* **2008**, *31*, 97.
[35] A. Varea, E. Pellicer, S. Pané, B. J. Nelson, S. Suriñach, M. D. Baró, J. Sort, *Int. J. Electrochem. Sci.* **2012**, *7*, 1288.
[36] C. Yang, W. Xue, H. Yin, Z. Lu, A. Wang, L. Shen, Y. Jiang, *New J. Chem.* **2017**, *41*, 3358.
[37] V. V. T. Padil, M. Černík, *Int. J. Nanomed.* **2013**, *8*, 889.
[38] M. Metikoš-Huković, R. Babić, I. Škugor, Z. Grubač, *Corros. Sci.* **2011**, *53*, 347.
[39] B. Younes, M.d. S. I. Sagar, A. I. Omi, N. R. Allison, D. Gedlick, P. K. Sekhar, *Prog. Electromagn. Res. B* **2022**, *95*, 103.
[40] H. Prajapati, N. N. Deshmukh, *Measurement* **2019**, *140*, 582.
[41] P. Seleghim Jr, in *Thermal Measurements and Inverse Techniques*, CRC Press, Boca Raton **2011**, 157.
[42] A. Sheng, S. Khuje, Z. Li, J. Yu, S. Ren, *ACS Appl. Electron. Mater.* **2022**, *4*, 5558.
[43] D. J. Lichtenwalner, A. E. Hydrick, A. I. Kingon, *Sens. Actuators, A* **2007**, *135*, 593.
[44] S. Khuje, A. Hehr, Z. Li, A. Krishnan, L. Kerwin, A. Kitt, J. Yu, S. Ren, *J. Mater. Eng. Perform.* **2021**, *30*, 5093.
[45] J. Cui, H. Liu, X. Li, S. Jiang, B. Zhang, Y. Song, W. Zhang, *Vacuum* **2020**, *176*, 109288.
[46] R. Phatthanakun, P. Deekla, W. Pummara, C. Sriphung, C. Pantong, N. Chomnawang, presented at 2012 7th IEEE International Conference on Nano/Micro Engineered and Molecular Systems (NEMS) **2012**.
[47] L. Shao, X. Zhao, S. Gu, Y. Ma, Y. Liu, X. Deng, H. Jiang, W. Zhang, *Vacuum* **2021**, *184*, 109966.
[48] G.-S. Chung, C.-H. Kim, *Microelectron. J.* **2008**, *39*, 1560.
[49] A. Maher, V. Velusamy, D. Riordan, J. Walsh, *Int. J. Smart Sens. Intell. Syst.* **2014**, *7*, 1.
[50] H. Y. Wang, W. J. Yang, D. W. Lee, Y. B. Kim, *Fuel Cells* **2014**, *14*, 626.
[51] C. Ahn, H. Park, H. Kim, S. Park, C. Son, M. Kim, J. Lee, J. Go, *J. Micromech. Microeng.* **2013**, *23*, 065031.
[52] V. B. Nam, D. Lee, *Nanomaterials* **2021**, *11*, 576.
[53] J. Martinez-Quijada, S. Caverhill-Godkewitsch, M. Reynolds, L. Gutierrez-Rivera, R. W. Johnstone, D. G. Elliott, D. Sameoto, C. J. Backhouse, *Sens. Actuators, A* **2013**, *193*, 170.